International Journal of Heat and Mass Transfer 51 (2008) 5359–5367

Contents lists available at ScienceDirect

International Journal of Heat and Mass Transfer

journal homepage: www.elsevier.com/locate/ijhmt

Thermal dispersion in porous media as a function of the solid–fluid conductivity ratio

Marcos H.J. Pedras [a], Marcelo J.S. de Lemos [b,*]

[a] EMBRAER, São José dos Campos – SP, Brazil
[b] Departamento de Energia – IEME, Instituto Tecnológico de Aeronáutica – ITA, 12228-900 São José dos Campos – SP, Brazil

ARTICLE INFO

Article history:
Received 24 May 2005
Received in revised form 1 April 2008
Available online 12 June 2008

Keywords:
Porous media
Thermal dispersion
Periodic boundary conditions
Low Reynolds k–ε model
Macroscopic energy equation

ABSTRACT

Thermal dispersion in porous media is an import phenomenon in combustion and in steam injection systems for Enhanced Oil Recovery methods, among several others engineering applications. In this work, thermal dispersion tensors were calculated within an infinite porous medium formed by a spatially periodic array of longitudinally-displaced elliptic rods. Two different thermal conductivity ratios between the solid and fluid phases were used for analyzing their effect on the thermal dispersion tensor, following a systematic analysis of several porous media modeled by different unit-cell geometry. As such, just one unit-cell, together with periodic boundary conditions for mass, momentum and energy equations, was used to represent the medium. The numerical methodology herein employed is based on the control-volume approach. Turbulence was assumed to exist within the fluid phase and a low Reynolds k–ε closure was used to model it. The flow equations at the pore-scale were numerically solved using the SIMPLE method on a non-orthogonal boundary-fitted coordinate system. Cell-integrated results for the longitudinal dispersion coefficient showed little sensitiveness on porosity, boundary condition type, medium morphology and solid–fluid conductivity ratio, whereas for the transversal direction, all of these parameters modified the numerical value obtained for the dispersion coefficient.

1. Introduction

Customarily, investigation of thermal dispersion in porous media makes use of the notion of representative elementary volume (REV) over which the transport equations are integrated [1–4]. These models, based on the macroscopic point of view, lose details on the flow pattern inside the REV and, together with ad-hoc information, provide global flow properties such as average velocities and temperatures. Recently, a number of papers can be found in the literature, which uses detailed macroscopic models for dispersion in porous media [5–8]. A REV is schematically represented in Fig. 1a.

On the other hand, flow in porous media can also be analyzed by modeling the topology of the medium and resolving the flow equations at the pore-scale. This treatment reveals the flow structure at the pore level an was used by [9–12] to determine the thermal dispersion tensors with periodic boundary conditions for mass, momentum and energy equations. Fig. 1b illustrates different model arrangements for a REV.

Following this second methodology, a systematic analysis on thermal dispersion in porous media has been carry out in Refs. [13–15] in order to contribute for the developing of a macroscopic transport equations based on the *double-decomposition* concept [16–22]. This systematic development has numerically investigated the thermal dispersion in beds modeled as arrays of cylindrical rods [13], longitudinally-displaced [14] and transversally-displaced [15] elliptic rods. In all of these investigations the thermal conductivity ratio between the solid and fluid phases was the same and their results were compared with several different geometries. The long term objective of such research effort is to investigate the effect of the thermal conductivity ratio between the solid and fluid phases on dispersive transport in highly permeable media.

The aim of the present contribution is to present thermal dispersion coefficients obtained in a medium modeled as an infinity array of longitudinally-displaced elliptic rods with two different thermal conductivity ratios between the solid and fluid phases, $k_s/k_f = 2$ and $k_s/k_f = 10$. Fig. 1c details the geometry under analysis and respective computational grid. Results for $k_s/k_f = 2$ were already presented by Ref. [14] whereas the results for $k_s/k_f = 10$ and the comparison between them will be presented in this work.

2. Microscopic equations

The thermal dispersion modeling and the macroscopic and microscopic equations herein utilized can be found in [13–15],

* Corresponding author.
E-mail address: delemos@ita.br (M.J.S. de Lemos).

0017-9310/$ - see front matter © 2008 Elsevier Ltd. All rights reserved.
doi:10.1016/j.ijheatmasstransfer.2008.04.030

Nomenclature

c_{pf}, c_{ps}	specific heat at constant pressure of fluid and solid
c_1, c_2, c_μ	dimensionless constants
f_2, f_μ	damping functions
H	characteristic length (Fig. 2)
k	turbulence kinetic energy
k_f, k_s	thermal conductivity of fluid and solid
$\mathbf{K}_{eff}$	effective conductivity
$\mathbf{K}_{tor}$	tortuosity tensor
$\mathbf{K}_{disp}$	dispersion tensor
n	coordinate normal to the wall
n_f, n_s	coordinate normal to the interface (Fig. 1)
Pe_H	Peclet number ($\lvert\langle\bar{\mathbf{u}}\rangle\rvert H/\alpha_f$)
T_f, T_s	temperature of fluid and solid
$\mathbf{u}$	local instantaneous (microscopic) velocity
u, v	components of $\mathbf{u}$

Greek symbols

ε	dissipation of k
γ	phase indicator (fluid f or solid s)
μ	dynamic viscosity
μ_t	turbulent viscosity
ν	kinematic viscosity
ν_t	turbulence (eddy) viscosity
ν_{t_ϕ}	macroscopic turbulence (eddy) viscosity
ρ_f, ρ_s	density
σ_k, σ_ε, σ_t	effective Prandtl number
ϕ_f	porosity or volume fraction of the fluid
ϕ_s	$1-\phi_f$ volume fraction of the solid

Special characters

$\bar{\varphi}_\gamma$	time average of $\varphi\gamma$
$\langle\varphi\gamma\rangle$	volume average of $\varphi\gamma$
$\langle\varphi\gamma\rangle^\gamma$	intrinsic average of $\varphi\gamma$ in the γ phase
φ'_γ	time fluctuation of $\varphi\gamma$
${}^i\varphi\gamma$	space deviation of $\varphi\gamma$

however for the sake of comprehensiveness some of those equations will be here presented once more.

The following microscopic transport equations describe the flow field and the heat transfer process within a porous medium,

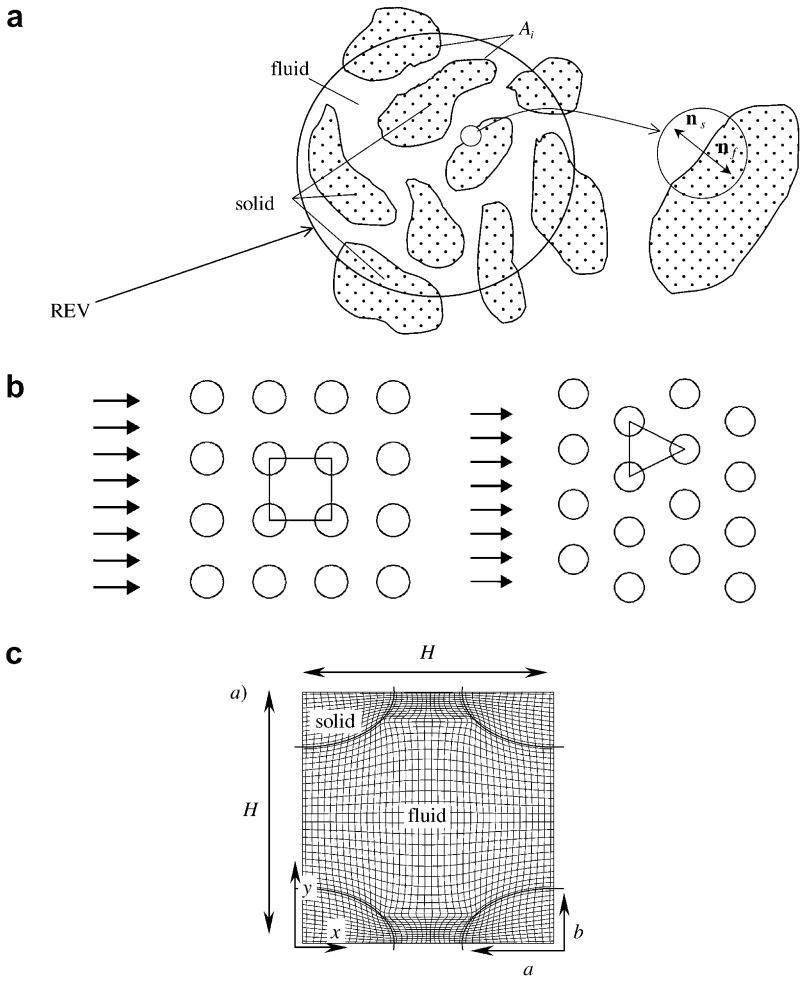

Fig. 1. (a) Representative elementary volume (REV), (b) square and staggered models for the REV and (c) unit-cell based on an infinite square arrangement of elliptic rods with $a/b = 5/3$ and computational grid.

where barred quantities represent time-averaged components and primes indicate turbulent fluctuations:

Fluid phase (incompressible fluid)

$$\nabla\cdot\bar{\mathbf{u}}=0 \tag{1}$$

$$\rho_f\left[\frac{\partial\bar{\mathbf{u}}}{\partial t}+\nabla\cdot(\bar{\mathbf{u}}\bar{\mathbf{u}})\right]=-\nabla\bar{p}+\nabla\cdot\{\mu[\nabla\bar{\mathbf{u}}+(\nabla\bar{\mathbf{u}})^{\mathrm{T}}]-\rho_f\overline{\mathbf{u}'\mathbf{u}'}\} \tag{2}$$

$$\rho_f c_{pf}\left[\frac{\partial\bar{T}_f}{\partial t}+\nabla\cdot(\bar{\mathbf{u}}\bar{T}_f)\right]=\nabla\cdot[k_f\nabla\bar{T}_f-\rho_f c_{pf}\overline{\mathbf{u}'T_f'}] \tag{3}$$

$$\rho_f\left[\frac{\partial k}{\partial t}+\nabla\cdot(\bar{\mathbf{u}}k)\right]=\nabla\cdot\left[\left(\mu+\frac{\mu_t}{\sigma_k}\right)\nabla k\right]-\rho_f\overline{\mathbf{u}'\mathbf{u}'}:\nabla\bar{\mathbf{u}}-\rho_f\varepsilon \tag{4}$$

$$\rho_f\left[\frac{\partial\varepsilon}{\partial t}+\nabla\cdot(\bar{\mathbf{u}}\varepsilon)\right]=\nabla\cdot\left[(\mu+\frac{\mu_t}{\sigma_\varepsilon})\nabla\varepsilon\right]+[c_1(-\rho_f\overline{\mathbf{u}'\mathbf{u}'}:\nabla\bar{\mathbf{u}})-c_2f_2\rho_f\varepsilon]\frac{\varepsilon}{k} \tag{5}$$

$$-\rho_f\overline{\mathbf{u}'\mathbf{u}'}=\mu_t[\nabla\bar{\mathbf{u}}+(\nabla\bar{\mathbf{u}})^{\mathrm{T}}]-\frac{2}{3}\rho_f k\mathbf{I} \tag{6}$$

$$-\rho_f c_{pf}\overline{\mathbf{u}'T_f'}=\rho_f c_{pf}\frac{\nu_t}{\sigma_t}\nabla\bar{T}_f \tag{7}$$

$$\mu_t=\rho_f\nu_t=\rho_f c_\mu f_\mu\frac{k^2}{\varepsilon} \tag{8}$$

Solid phase

$$\rho_s c_{ps}\frac{\partial\bar{T}_s}{\partial t}=\nabla\cdot[k_s\nabla\bar{T}_s] \tag{9}$$

where $\mathbf{u}$ is the microscopic velocity, ρ_f and ρ_s the fluid and solid densities, p the thermodynamic pressure, μ and μ_t the dynamic and turbulent viscosities, T_f and T_s the fluid and solid temperatures, c_{pf} and c_{ps} the fluid and solid specific heat at constant pressure, k_f and k_s the fluid and solid thermal conductivities, k the turbulent kinetic energy and ε the dissipation of k. In the equations σ_k, σ_ε and σ_t are effective Prandtl numbers, c_1, c_2 and c_μ are dimensionless constants and f_2 and f_μ damping functions.

To account for turbulence the low Reynolds k–ε closure was applied, utilizing the damping functions and model constants of [23].

For the unit-cell represented in Fig. 1c, and with the assumption of macroscopic fully developed uni-dimensional flow, the interfacial (fluid/solid) conditions at the walls are,

$$\bar{\mathbf{u}}=0;\ \bar{T}_f=\bar{T}_s;\ \mathbf{n}_f\cdot(k_f\nabla\bar{T}_f)=-\mathbf{n}_s\cdot(k_s\nabla\bar{T}_s);$$
$$k=0\quad\text{and}\quad\varepsilon=\nu\frac{\partial^2k}{\partial n^2}, \tag{10}$$

Unit-cell boundary conditions for the hydrodynamic field follow a periodic condition as follow:

on $x=0$ and $x=H$,

$$\bar{u}|_{x=0}=\bar{u}|_{x=H},\quad\bar{v}|_{x=0}=\bar{v}|_{x=H},\quad k|_{x=0}=k|_{x=H}$$
$$\text{and}\quad\varepsilon|_{x=0}=\varepsilon|_{x=H} \tag{11}$$

on $y=0$ and $y=H$,

$$\frac{\partial\bar{u}}{\partial y}=\frac{\partial\bar{v}}{\partial y}=\frac{\partial k}{\partial y}=\frac{\partial\varepsilon}{\partial y}=0 \tag{12}$$

where n_f and n_s are the coordinates normal to the interface (Fig. 1a) and u and v the components of $\mathbf{u}$. Temperature boundary conditions will be presented in the next section.

3. Thermal dispersion modeling

The thermal dispersion modeling utilized in this work follows the same procedure of [13–15]. The macroscopic energy equation is obtained by volume averaging the microscopic energy equations (3) and (9) over the REV of Fig. 1a assuming local thermal equilibrium assumption, i.e., $\langle\bar{T}_f\rangle^f=\langle\bar{T}_s\rangle^s=\langle\bar{T}\rangle$. The result is

$$[\phi_f\rho_f c_{pf}+\phi_s\rho_s c_{ps}]\frac{\partial\langle\bar{T}\rangle}{\partial t}+\rho_f c_{pf}\nabla\cdot(\langle\bar{\mathbf{u}}\rangle\langle\bar{T}\rangle)=\nabla\cdot\mathbf{K}_{\mathrm{eff}}\cdot\nabla\langle\bar{T}\rangle \tag{13}$$

where $\langle\bar{T}\rangle$ is the volume average of the time averaged temperature, $\langle\bar{T}_\gamma\rangle^\gamma$ the intrinsic average of the time-averaged temperature in the γ phase, ϕ_f the volume fraction of fluid and $\phi_s=1-\phi_f$ the volume fraction of solid. The effective conductivity, $\mathbf{K}_{\mathrm{eff}}$, the tortuosity tensor, $\mathbf{K}_{\mathrm{tor}}$, and the dispersion tensor, $\mathbf{K}_{\mathrm{disp}}$, are defined as

$$\mathbf{K}_{\mathrm{eff}}=(\phi_f\frac{\rho_f c_{pf}\nu_{t_\phi}}{\sigma_t}+\phi_f k_f+\phi_s k_s)\mathbf{I}+\mathbf{K}_{\mathrm{tor}}+\mathbf{K}_{\mathrm{dis}} \tag{14}$$

$$\mathbf{K}_{\mathrm{tor}}\cdot\nabla\langle\bar{T}\rangle=\frac{(k_f-k_s)}{\Delta V}\int_{A_i}\mathbf{n}_f{}^i\bar{T}_f\,\mathrm{d}S \tag{15}$$

$$\mathbf{K}_{\mathrm{disp}}\cdot\nabla\langle\bar{T}\rangle=-\rho_f c_{pf}\phi_f\langle{}^i\bar{\mathbf{u}}{}^i\bar{T}_f\rangle^f=-\frac{\rho_f c_{pf}}{\Delta V}\int_{\Delta V_f}{}^i\bar{\mathbf{u}}{}^i\bar{T}_f\,\mathrm{d}V \tag{16}$$

where ${}^i\varphi$ is the space deviation of φ

According to Fig. 2a, the macroscopic velocity and temperature gradients are given by

$$\langle\bar{\mathbf{u}}\rangle^v=|\langle\bar{\mathbf{u}}\rangle^v|(\cos\theta\vec{i}+\sin\theta\vec{j}) \tag{17}$$

$$\nabla\langle\bar{T}\rangle=\frac{\Delta T}{H}(-\sin\theta\vec{i}+\cos\theta\vec{j})-\text{transversal component} \tag{18}$$

$$\nabla\langle\bar{T}\rangle=\frac{\Delta T}{H}(\cos\theta\vec{i}+\sin\theta\vec{j})-\text{longitudinal component} \tag{19}$$

If the gradient of the average temperature is in the same direction of the macroscopic flow or transverse to it, only diagonal components of $\mathbf{K}_{\mathrm{dis}}$ remain non-zero components. In these conditions, Eq. (16) renders, respectively, for the diagonal components of $\mathbf{K}_{\mathrm{dis}}$,

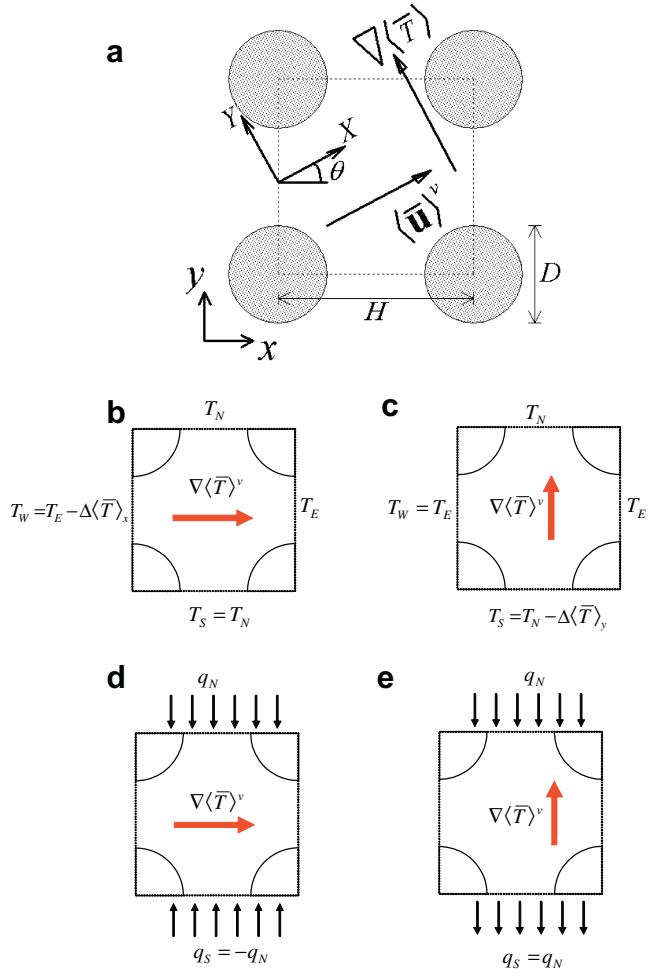

Fig. 2. Unit-cell and boundary conditions: (a) macroscopic velocity and temperature gradients; *given temperature difference* at East–West boundaries, (b) *longitudinal* gradient, Eq. (24), (c) *transversal* gradient, Eq. (25); *Given heat fluxes* at North–South boundaries, (d) *longitudinal* gradient and (e) *transversal* gradient.

$$(K_{\mathrm{dis}})_{xx} \approx -\frac{\frac{\rho_{\mathrm{f}} c_{\mathrm{pf}}}{\Delta V}}{\frac{\Delta\langle\overline{T}\rangle_x}{H}} \int_{\Delta V_{\mathrm{f}}} {}^{i}\bar{u}^{i}\overline{T}_{\mathrm{f}}\,\mathrm{d}V \tag{20}$$

or

$$(K_{\mathrm{dis}})_{xx} \approx -\frac{\frac{\rho_{\mathrm{f}} c_{\mathrm{pf}}}{\Delta V}}{\frac{\Delta\langle\overline{T}\rangle_x}{H}} \int_0^H \int_0^H \left(\bar{\mathbf{u}} - \langle\bar{\mathbf{u}}\rangle^{i}\right)\left(\overline{T} - \langle\overline{T}\rangle\right)\mathrm{d}x\,\mathrm{d}y \cdot (\cos\theta\vec{i} + \sin\theta\vec{j}) \tag{21}$$

and

$$(K_{\mathrm{dis}})_{yy} \approx -\frac{\frac{\rho_{\mathrm{f}} c_{\mathrm{pf}}}{\Delta V}}{\frac{\Delta\langle\overline{T}\rangle_y}{H}} \int_{\Delta V_{\mathrm{f}}} {}^{i}\bar{v}^{i}\overline{T}_{\mathrm{f}}\,\mathrm{d}V \tag{22}$$

or

$$(K_{\mathrm{dis}})_{yy} \approx -\frac{\frac{\rho_{\mathrm{f}} c_{\mathrm{pf}}}{\Delta V}}{\frac{\Delta\langle\overline{T}\rangle_y}{H}} \int_0^H \int_0^H (\bar{\mathbf{u}} - \langle\bar{\mathbf{u}}\rangle^{i})(\overline{T} - \langle\overline{T}\rangle)\,\mathrm{d}x\,\mathrm{d}y \cdot (-\sin\theta\vec{i} + \cos\theta\vec{j}) \tag{23}$$

Solution of the flow and energy equations inside the unit-cell provides the velocity and temperature distributions necessary for the integrands of (20) and (22). These values are needed in order to calculate the dispersion components. Further, in (20) and (22) the gradients $\Delta\langle\overline{T}\rangle_x$ and $\Delta\langle\overline{T}\rangle_y$ can be calculated in two ways, as presented next.

4. Imposed boundary temperature difference

In the first method, a temperature difference or Dirichlet boundary conditions are imposed for the energy equation at the faces of the computational cell [10,12] as shown below.

As mentioned, two distinct macroscopic temperature gradients are considered to obtain the transverse and longitudinal dispersion coefficients (20) and (22), respectively.

Following [10], we impose a macroscopically linear temperature gradient along with the macroscopic flow for obtaining $(K_{\mathrm{dis}})_{xx}$ so that (see Fig. 2b),

$$\overline{T}_{x=0} = \overline{T}_{x=H} - \Delta\langle\overline{T}\rangle_x \quad \text{and} \quad \overline{T}_{y=0} = \overline{T}_{y=H} \tag{24}$$

For the $(K_{\mathrm{dis}})_{yy}$ calculation, one has (Fig. 2c),

$$\overline{T}_{x=0} = \overline{T}_{x=H} \quad \text{and} \quad \overline{T}_{y=0} = \overline{T}_{y=H} - \Delta\langle\overline{T}\rangle_y \tag{25}$$

In both Eqs. (24) and (25), $\Delta\langle\overline{T}\rangle_x$ and $\Delta\langle\overline{T}\rangle_y$ are given constants. All temperatures at the four boundaries are iteratively modified, along the relaxation process, subjected to the constraints given by Eqs. (24) and (25). With such imposed temperature at the boundaries, energy Eqs. (3) and (9) are numerically solved and residues are brought down below a pre-selected tolerance.

5. Imposed boundary heat flux

The other possibility for getting a macroscopic temperature difference across the cell, in either the longitudinal direction for having $\Delta\langle\overline{T}\rangle_x$ to be used in (20), or for calculating $\Delta\langle\overline{T}\rangle_y$ for applying it in (22), is to impose heat fluxes at the north and south boundaries of the unit-cell shown in Fig. 2a. When the two fluxes "enter" the cell (Fig. 2d), $\Delta\langle\overline{T}\rangle_x$ is obtained. For heat entering from above and leaving at the south surface, the situation is analogous of having a uniform transverse temperature difference $\Delta\langle\overline{T}\rangle_y$ across the y-direction (Fig. 2e).

In those cases, $\Delta\langle\overline{T}\rangle_x$ and $\Delta\langle\overline{T}\rangle_y$ are no longer given values, but rather a consequence of the imposed heat fluxes (Newman conditions) at the north and south boundaries. Their values are then calculated as,

$$\Delta\langle\overline{T}\rangle_x = \frac{1}{H}\int_{y=0}^{y=H} [\overline{T}_{x=H} - \overline{T}_{x=0}]\,\mathrm{d}y \tag{26}$$

$$\Delta\langle\overline{T}\rangle_y = \frac{1}{H}\int_{x=0}^{x=H} [\overline{T}_{y=H} - \overline{T}_{y=0}]\,\mathrm{d}x \tag{27}$$

It is important to highlight the equivalence of the pairs of Eqs. (24)–(26) and (25)–(27). One should emphasize that distributed temperatures are computed first within the cell in Fig. 2, which are therefore obtained at the pore level, without resorting to any macroscopic view. Accordingly, at the pore level, one identifies only diffusion (laminar/turbulent) and convection as the existing mechanisms for transporting heat to and out of the unit-cell of Fig. 2. Mechanisms such as **dispersion** and **tortuosity** entail operations over the entire REV and, as such, they are not defined at the pore level, and are rather the outcome of macroscopic models, which are identified by Eqs. (15) and (16), respectively. At the pore level, or say within the domain in Fig. 2, only diffusion and convection heat transport are present.

Accordingly, when imposing Eq. (24) (Fig. 2b), temperature values at the north and south face are iteratively adjusted, subjected to condition $\overline{T}_{y=0} = \overline{T}_{y=H}$ for $0 < x < H$, so that their gradients at both boundaries will be such that corresponding heat fluxes entering the unit-cell will satisfy the energy balance and will match the convected energy leaving at the east face. Therefore, after achieving the numerical solution of Eqs. (3) and (9), the sum of heat fluxes at east, north and south boundaries match that leaving the cell at east.

Local heat fluxes at north and south faces present a longitudinal distribution along the x-direction and are given, at the north face for the gap between rods ($y = H$, $D/2 < x < H - D/2$), as follows,

$$q^{\mathrm{calc}}_{y=H} = \underbrace{-\left(k_{\mathrm{f}} + \frac{c_{\mathrm{pf}}\mu_{\mathrm{t}}}{\sigma_{\mathrm{t}}}\right)\left.\frac{\partial\overline{T}}{\partial y}\right|_{y=H}}_{\text{conduction and turbulent diffusion}} + \underbrace{\rho_{\mathrm{f}} c_{\mathrm{pf}}(v\overline{T})_{y=H}}_{\text{convection}} \tag{28}$$

Across the solid phase at the same north-boundary, $\mu_{\mathrm{t}} = 0$ and $v = 0$ and the calculated north-boundary heat flux becomes,

$$q^{\mathrm{calc}}_{y=H} = \underbrace{-k_{\mathrm{s}}\left.\frac{\partial\overline{T}}{\partial y}\right|_{y=H}}_{\text{conduction}} \tag{29}$$

On the other hand, by imposing a given value for $q_{y=H}$, instead of calculating it via Eq. (28) (see Fig. 2d), temperatures at the north cell face $\overline{T}_{y=H}$ will be adjusted such that,

$$q^{\mathrm{given}}_{y=H} = -\left.\left(k_{\mathrm{f}} + \frac{c_{\mathrm{pf}}\mu_{\mathrm{t}}}{\sigma_{\mathrm{t}}}\right)\frac{(\overline{T}_{y=H} - \overline{T}_{\mathrm{B}})}{\delta y}\right|_{y=H} + \rho_{\mathrm{f}} c_{\mathrm{pf}}(v\overline{T})_{y=H} \tag{30}$$

where $\overline{T}_{\mathrm{B}}$ represents the temperature at the computational node closest to the boundary, which is located at a distance δy from it. An explicit equation for $\overline{T}_{y=H}$ can then be obtained as

$$\overline{T}_{y=H} = \frac{q^{\mathrm{given}}_{y=H} - \left.\left(k_{\mathrm{f}} + \frac{c_{\mathrm{pf}}\mu_{\mathrm{t}}}{\sigma_{\mathrm{t}}}\right)\overline{T}_{\mathrm{B}}\right|_{y=H}}{\left[-\left(k_{\mathrm{f}} + \frac{c_{\mathrm{pf}}\mu_{\mathrm{t}}}{\sigma_{\mathrm{t}}}\right)\frac{1}{\delta y} + \rho_{\mathrm{f}} c_{\mathrm{pf}} v\right]_{y=H}} \tag{31}$$

For the south face one has

$$\overline{T}_{y=0} = \frac{q^{\mathrm{given}}_{y=0} + \left.\left(k_{\mathrm{f}} + \frac{c_{\mathrm{pf}}\mu_{\mathrm{t}}}{\sigma_{\mathrm{t}}}\right)\overline{T}_{\mathrm{B}}\right|_{y=0}}{\left[\left(k_{\mathrm{f}} + \frac{c_{\mathrm{pf}}\mu_{\mathrm{t}}}{\sigma_{\mathrm{t}}}\right)\frac{1}{\delta y} + \rho_{\mathrm{f}} c_{\mathrm{pf}} v\right]_{y=0}} \tag{32}$$

Invoking symmetry condition about the plane $y = H/2$, as shown in Fig. 2d, one gets $q^{\mathrm{given}}_{y=0} = -q^{\mathrm{given}}_{y=H}$ and $v_{y=0} = -v_{y=H}$, which, in turn, result in Eq. (24) ($\overline{T}_{y=0} = \overline{T}_{y=H}$), after comparing Eqs. (31) and (32).

Further, once temperatures at all four faces are updated at each iteration, a convenient longitudinal temperature drop is calculated

by Eq. (26), instead of being imposed as schematically shown in Fig. 2b. Similar arguments can be said about the equivalence of conditions (25) (Fig. 2c) and (27) (Fig. 2e). Additional comments on the relaxation procedure are shown next.

6. Numerical model

The transport equations at the pore-scale were numerically solved using the SIMPLE method on a non-orthogonal boundary-fitted coordinate system. The equations were discretized using the finite volume procedure of [24]. The relaxation process starts with the solution of the two momentum equations and the velocity fields is adjusted in order to satisfy the continuity principle. This adjustment is attained by solving the pressure correction equation. The turbulence model and the energy equations are relaxed to update the k, ε and temperature fields. Details on the numerical discretization can be found in [18].

In this work just one unit-cell, together with periodic boundary conditions for mass, momentum and Neumann and Dirichlet conditions for the energy equation, was used to represent the porous medium. In all runs, flow was always in the horizontal direction and from left to right. For given $\Delta\langle\overline{T}\rangle_x$ and $\Delta\langle\overline{T}\rangle_y$ in Fig. 2b and c, respectively, all boundary temperatures were varied during the relaxation process until all equations converged. For the Neumann temperature conditions (Fig. 2d and e), the thermal dispersion tensors were calculated after a sequence of converged loops on the same run. This sequence of loops followed the same procedure detailed in [17]. After convergence with initial profiles at the west faces, outlet profiles at $x=H$ were plugged back at the inlet in $x = 0$. Although the volume average temperature $\langle\overline{T}\rangle^v$ changed after increasing the inlet temperature profile in each run, the spatial deviation temperature field ${}^vT = T - \langle\overline{T}\rangle^v$ within the cell becomes established as the flow develops along the x-direction. In this situation, the flow is considered to have a macroscopically developed thermal field.

Also, in the low Re model, the node adjacent to the wall requires that $u_\tau n/\nu \leqslant 1$. To accomplish this requirement, the grid needs points close to the wall leading to computational meshes of 40×54 nodes. A highly non-uniform grid arrangement was employed with concentration of nodes close to the wall. Values for $(K_{dis})_{xx}$ and $(K_{dis})_{yy}$ were obtained varying the $Pe_H = |\langle\bar{\mathbf{u}}\rangle|H/\alpha_f$ from 10^0 to 4×10^3 and the $\phi_f = 1 - ab\pi/H^2$, from 0.60 to 0.90 [25,26].

7. Results and discussion

A total of 27 runs were carried out being 23 for laminar flow and four for turbulent flow with the low Re model theory. In all runs it was used for the fluid phase a Prandtl number of 0.72 and a thermal conductivity ratio between the solid and fluid phase of $k_s/k_f = 10$.

Temperature fields calculated with given boundary temperatures conditions sketched in Fig. 2b (see Eq. (24)) are presented in the Fig. 3a and b, for $Pe_H = 10$ and 4×10^3, respectively. On the other hand, results for the same cases but using the given flux boundary type of Fig. 2d are shown in Fig. 3c and d for the same Pe_H numbers. In all Fig. 3, the macroscopic temperature gradient $\nabla\langle\overline{T}\rangle^v$ is in the same horizontal direction as the macroscopic flow $\langle\bar{\mathbf{u}}\rangle^v$. As will be shown further, in spite of the differences in temperature fields, obtained mainly in the solid phase, the values of the longitudinal component of $\mathbf{K}_{dis}$ were very similar. This behavior can be explained by recalling the definition of the $\mathbf{K}_{dis}$ (Eq. (16)), i.e., the determination of $\mathbf{K}_{dis}$ is dependent on the deviation fields

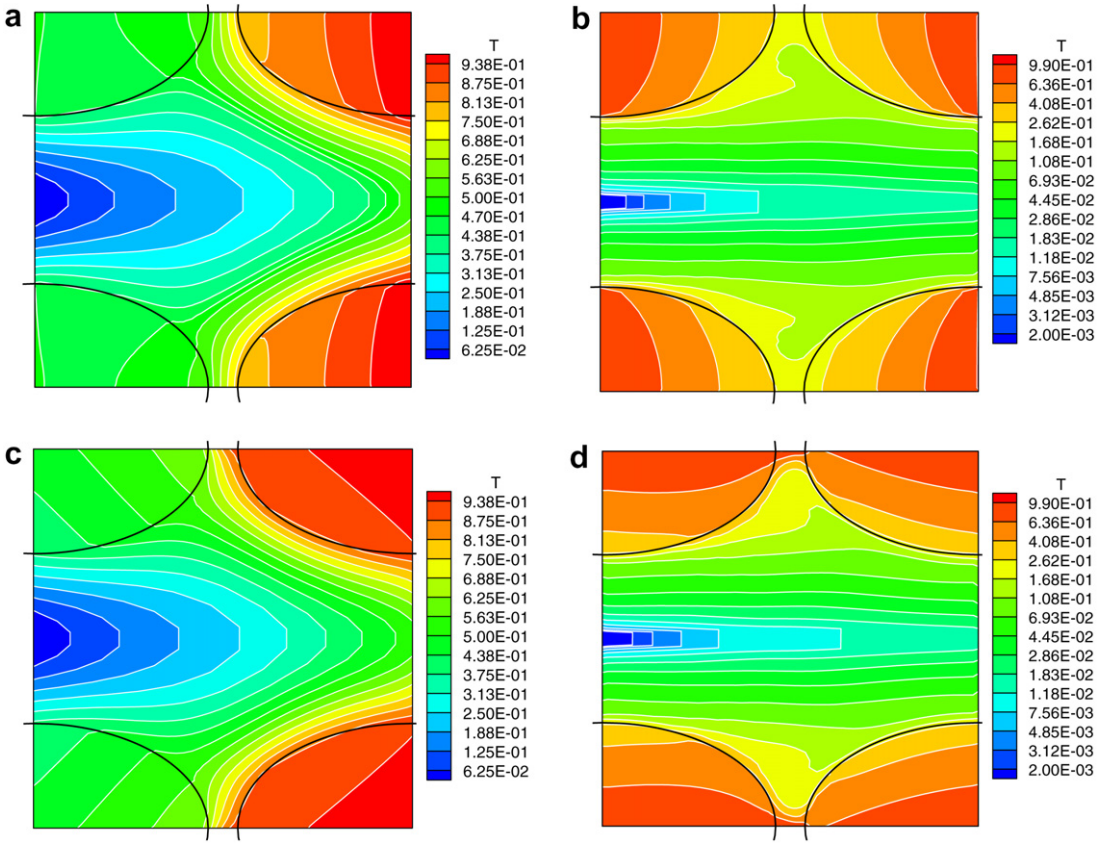

Fig. 3. Temperature field with imposed *longitudinal* temperature gradient, $\phi_f = 0.60$: *Given temperature difference* at East–West boundaries (see Eq. (24)), (a) $Pe_H = 10$, (b) $Pe_H = 4 \times 10^3$; *Given heat fluxes* at North–South boundaries (see Fig. 2d), (c) $Pe_H = 10$ and (d) $Pe_H = 4 \times 10^3$.

of velocity and temperature within the fluid phase. As such, inspecting Fig. 3a and c for small Peclet and Fig. 3b and d for $Pe_H = 4 \times 10^3$, one can see that velocity and temperature fields within the fluid phase, regardless of the boundary type used, resembles fairly well each other.

Temperature fields calculated with boundary conditions sketched in Fig. 2c (Eq. (25)) and in Fig. 2d are presented, respectively, in the Fig. 4a and c for $Pe_H = 10$ and in Fig. 4b and d for $Pe_H = 4 \times 10^3$. In Fig. 4 $\nabla\langle\overline{T}\rangle^v$ is transversal to $\langle\bar{\mathbf{u}}\rangle^v$. Also here the temperature files obtained with the two methodologies, namely given boundary T values or heat fluxes, are close to each other. As before, here also the transverse component of $\mathbf{K}_{\text{dis}}$ calculated with these two boundary conditions will be very close to one another, as will be seen below. Furthermore, as Pe_H increases, Fig. 4a–d shows the same behavior of Fig. 3a–d, i.e., as the flow rate increases, the fluid temperature becomes more homogeneous due to enhancement of the convection strength.

Fig. 5 shows the longitudinal component of the thermal dispersion tensor as a function of the Peclet number (Fig. 5a) and for different porosities (Fig. 5b). Results in Fig. 5a show good agreement when compared with the data of [10,12], for square and cylindrical rods, respectively, and for the same porosity. Also, a mentioned before, the use of different boundary conditions (Fig. 2b and d) yields very little differences in the longitudinal component of $(\mathbf{K}_{\text{dis}})_{xx}$. Fig 5a also shows that for different medium morphologies (longitudinal-displaced elliptic, square and cylindrical rods), $(\mathbf{K}_{\text{dis}})_{xx}$ is little sensitive. For the same fluid, Pe_H and porosity, the mass flow rate through the bed will be the same. Thus, the overall convection strength and temperatures along the x-direction will vary little, which, in turn, will yield similar values for $(\mathbf{K}_{\text{dis}})_{xx}$.

Fig. 5b presents longitudinal dispersion coefficients for porosities covering the range 0.6–0.9. For lower Peclet number, applications of both boundary conditions result in nearly the same values for $(\mathbf{K}_{\text{dis}})_{xx}$. Also for higher Pe_H, dependency of $(\mathbf{K}_{\text{dis}})_{xx}$ with ϕ is small. On the overall, for all porosities here considered, a general equation indicating the dependence of longitudinal thermal dispersion on Peclet can be inferred as

$$(K_{\text{dis}})_{xx}/k_{\text{f}} = 3.45 \times 10^{-2} Pe_H^{1.65} \tag{33}$$

showing, as expected, the usual behavior of $(K_{\text{dis}})_{xx}/k_{\text{f}} \sim Pe_H^n$.

The longitudinal components calculated with $k_{\text{s}}/k_{\text{f}} = 2$ was given in [14] as

$$(K_{\text{dis}})_{xx}/k_{\text{f}} = 3.52 \times 10^{-2} Pe_H^{1.65} \tag{34}$$

These results are plotted in Fig. 6a with those calculated with $k_{\text{s}}/k_{\text{f}} = 10$. On can see that the conductivity ratio $k_{\text{s}}/k_{\text{f}}$ has little influence on the behavior of the $(K_{\text{dis}})_{xx} \times Pe_H^{1.65}$ curve. Temperatures inside the solid will be mostly affected by increasing the solid thermal conductivity and, as seen before, $(K_{\text{dis}})_{xx}$ values are basically dependent on the fluid phase temperature (see Eq. (20)).

The transverse component of the thermal dispersion, $(K_{\text{dis}})_{yy}$, is shown next in Fig. 7. As already mentioned, the use of different boundary conditions (Fig. 2c and e) yields very little differences in the transverse component of the dispersion tensor $\mathbf{K}_{\text{dis}}$. However, in Fig. 7a one can also see that different medium morphologies, such as longitudinal-displaced elliptic rods (present results), as well as square [10] and cylindrical rods [12], yield substantially different values for $(K_{\text{dis}})_{yy}$. Results for square rods by [10] were greater than for circular rods [12], which were further greater than the present results. If one recall that $(K_{\text{dis}})_{yy}$ is associated with

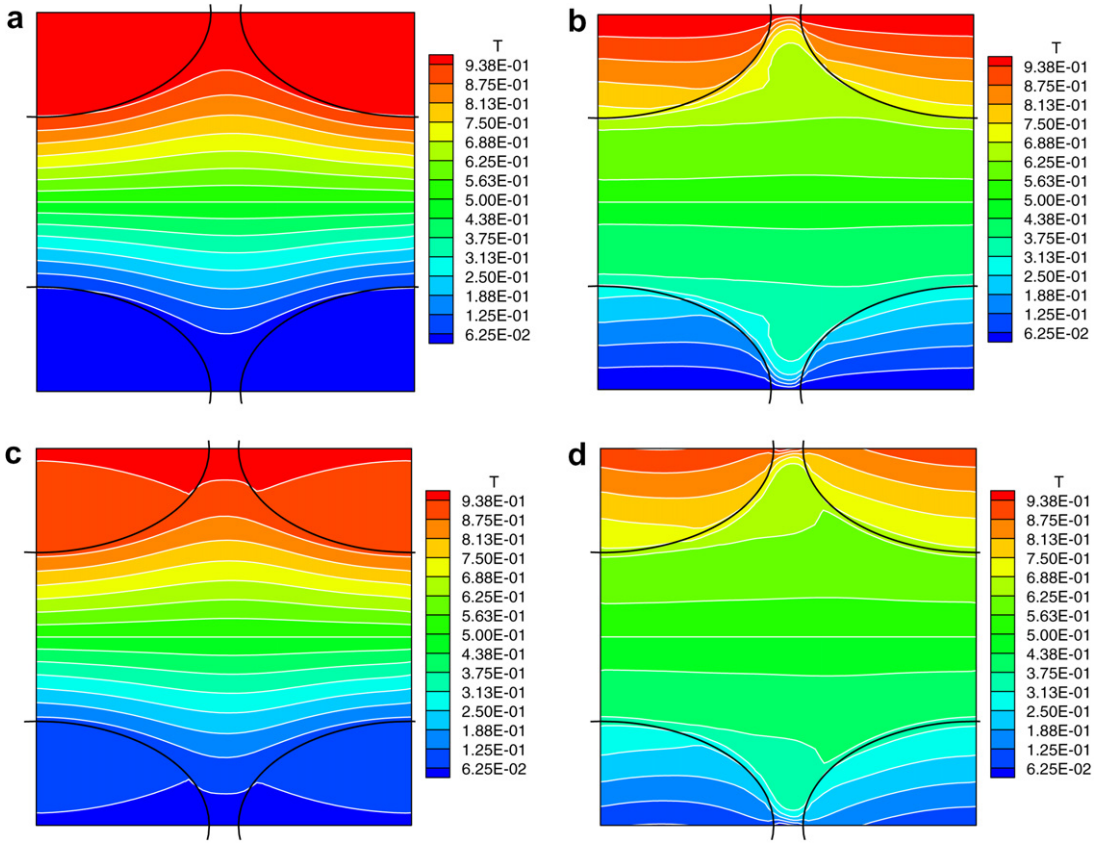

Fig. 4. Temperature field with imposed *transversal* temperature gradient, $\phi_{\text{f}} = 0.60$: *Given temperature difference* at North–South boundaries (see Eq. (25)), (a) $Pe_H = 10$, (b) $Pe_H = 4 \times 10^3$; *Given heat fluxes* at North–South boundaries (see Fig. 2e), (c) $Pe_H = 10$ and (d) $Pe_H = 4 \times 10^3$.

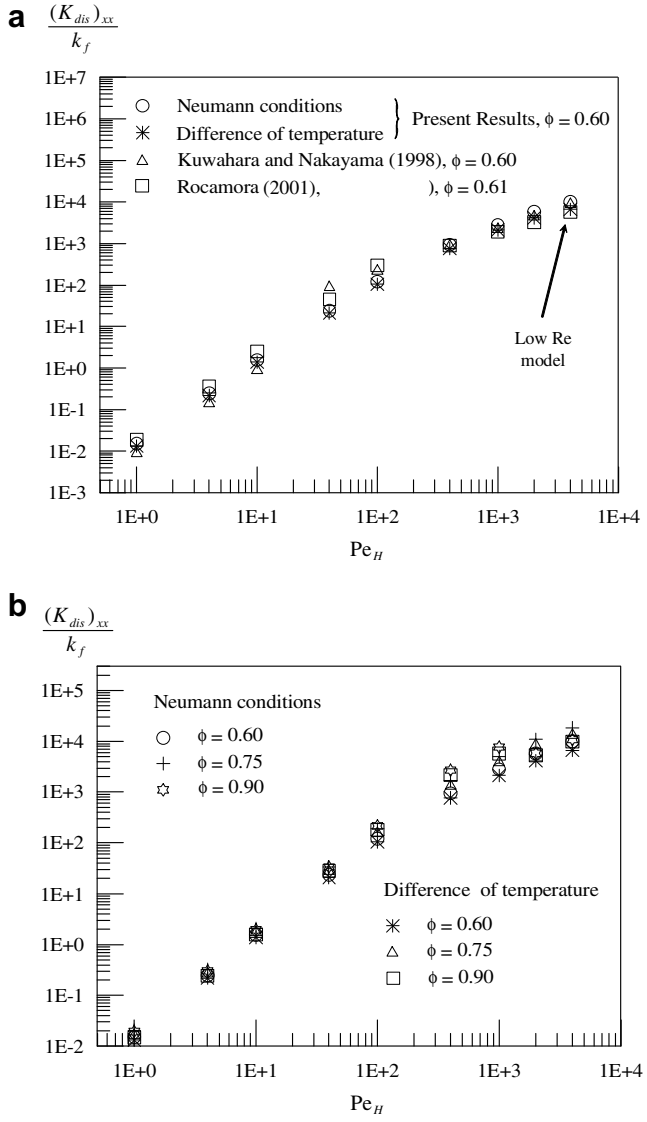

Fig. 5. Longitudinal thermal dispersion: (a) $\phi_f = 0.60$ and (b) overall results.

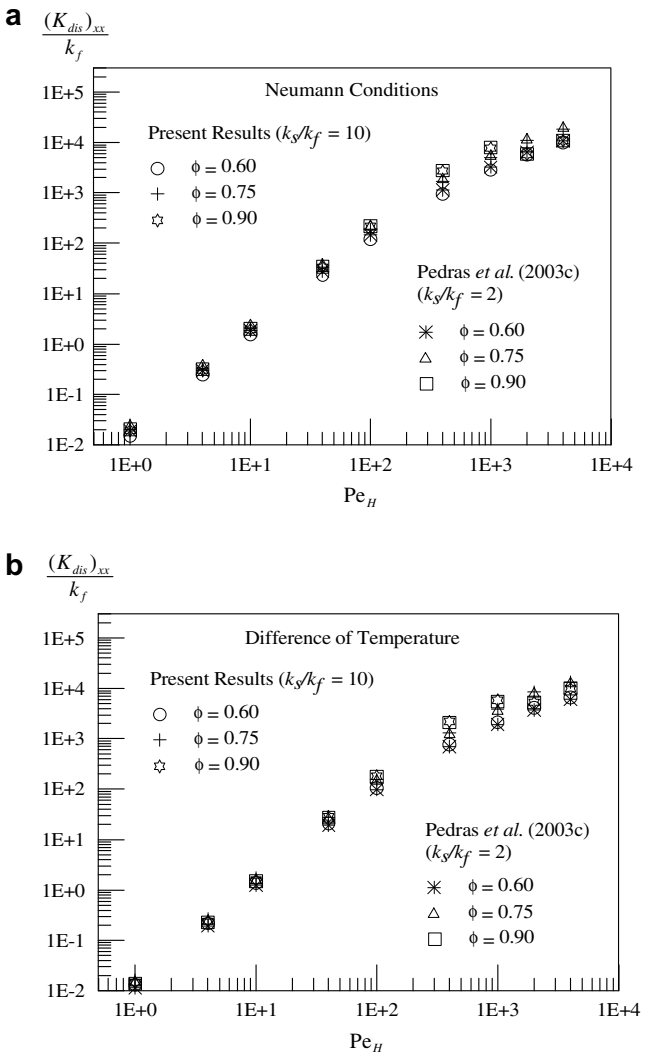

Fig. 6. *Longitudinal* thermal dispersion comparing between $k_s/k_f = 2$ and $k_s/k_f = 10$: (a) Neumann boundary conditions, Fig. 2d; (b) temperature boundary conditions, Fig. 2b; Eq. (24).

dispersive transport in the *y*-direction, one can infer that the easier the fluid flows in the longitudinal *x*-direction, due to a streamwise optimized geometric shape, for example (longitudinally-displayed elliptic rods), less exchange in the transversal direction will take place. Also, for the same porosity or void-to-cell volume ratio, square, cylindrical and elliptical rods will have a reducing opening area in the north and south faces of the unit-cell (see Fig. 2a), reducing them the exchange of energy in the transverse *y*-direction. It is also interesting to point out that $(K_{dis})_{yy}$ is several order of magnitude smaller than $(K_{dis})_{xx}$ due to the fact that for a macroscopically horizontal flow most dispersive transport will be along the main flow direction. The overall dependence of the transverse component on the Peclet number was found to be

$$(K_{dis})_{yy}/k_f = 1.55 \times 10^{-4} Pe_H^{0.94} \quad (35)$$

Fig. 7b further shows the dependence of $(K_{dis})_{yy}$ with the porosity ϕ for the case here investigated, namely the longitudinally-displaced elliptic rods. Results confirm the already observed insensitivity of the results on the type of boundary condition used. Dependency on the porosity of the cell is more difficult to access due to the spread of the results. Nevertheless, a general observation can be made that by reducingϕ, via increasing the size of the ellipses, lower values for $(K_{dis})_{yy}$ are obtained, at least for low Pe_H. This observation is in line with an argument already used that the more obstructed the passages are in between cells along *y*, the lower the values of $(K_{dis})_{yy}$ will be.

Fig. 8 finally shows comparisons between the transverse components calculated with $k_s/k_f = 2$ [14], where

$$(K_{dis})_{yy}/k_f = 2.29 \times 10^{-4} Pe_H^{0.88} \quad (36)$$

with the cases having $k_s/k_f = 10$. The comparison shows that the transverse component is more sensible to the variation of the conductivity ratio than the longitudinal component, In general, for higher k_s/k_f ratios, lower $(K_{dis})_{yy}/k_f$ coefficients were obtained. Such difference mainly occur for Peclet about 10^2. In this range of Pe_H, little recirculation was observed behind the rods (not shown here). A possible explanation for this behavior might be associated with the temperature deviation values ${}^iT$ existing in the fluid, in each case. For $k_s/k_f = 2$, temperature gradients in the recirculating zones (behind the rods in the *x*-direction) was larger that those for $k_s/k_f = 10$, which, in turn, were almost negligible. This almost zero temperature gradient along with the recirculating zone for $k_s/k_f = 10$ reduced the temperature deviations ${}^iT$, which, from Eq. (22), reduced the transverse dispersion.

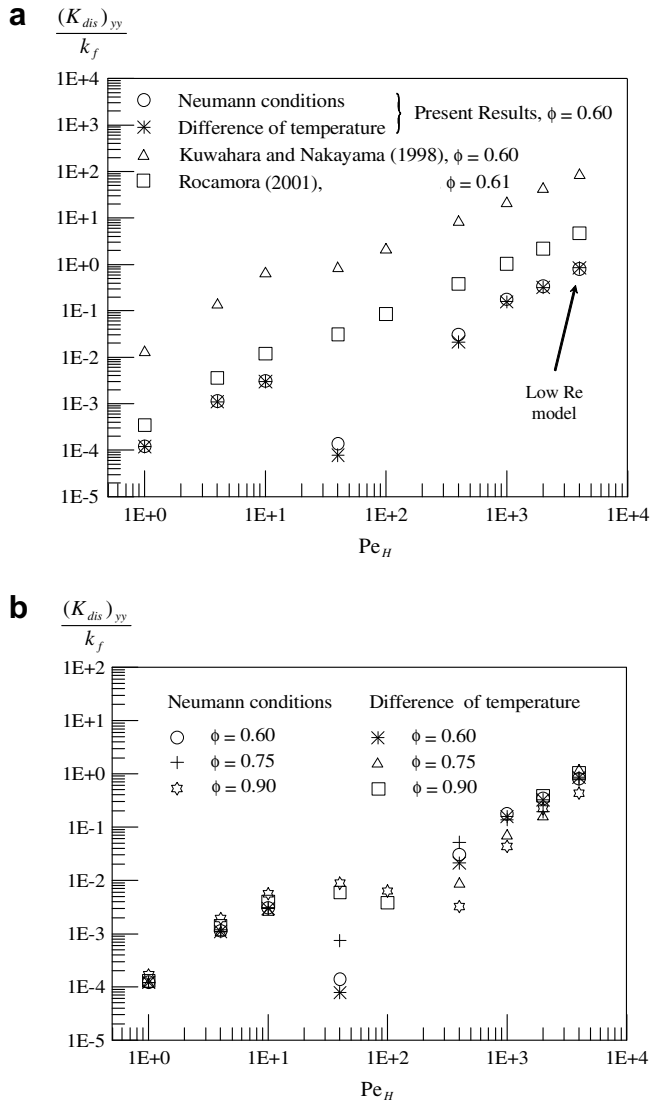

Fig. 7. Transverse thermal dispersion: (a) $\phi_f = 0.60$ and (b) overall results.

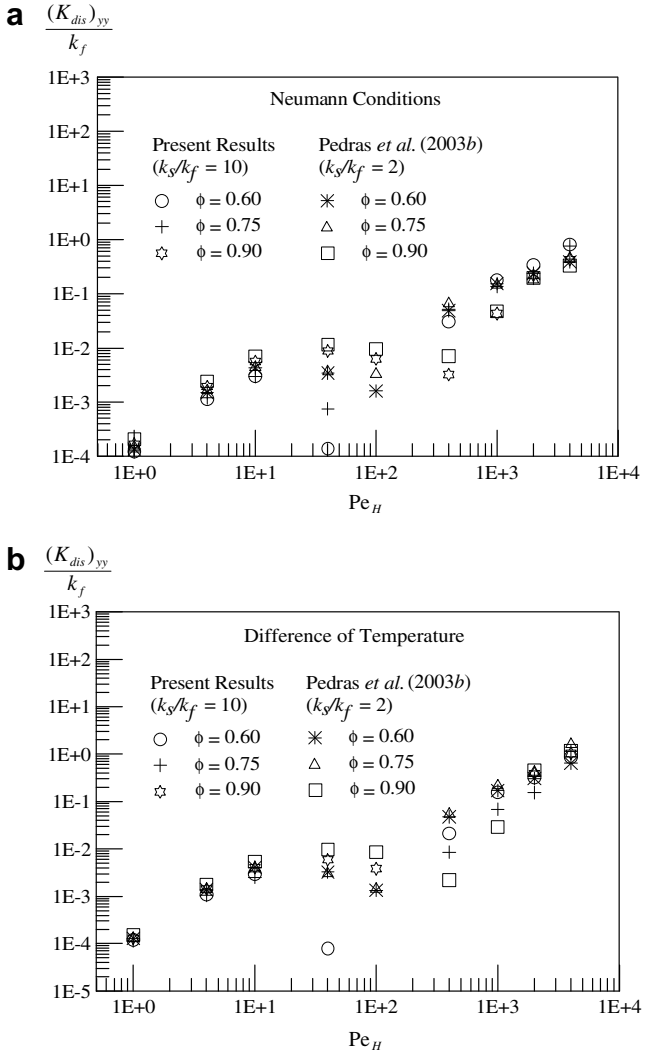

Fig. 8. *Transverse* thermal dispersion comparing between $k_s/k_f = 2$ and $k_s/k_f = 10$: (a) Neumann boundary conditions, Fig. 2e; (b) temperature boundary conditions, Fig. 2c, Eq. (25).

8. Conclusions

Results of thermal dispersion components $(K_{dis})_{xx}$ and $(K_{dis})_{yy}$, calculated for a periodic porous medium modeled as an infinite array of longitudinally-displaced elliptic rods, where presented for porosity in the range $0.6 < \phi < 0.9$ and thermal conductivity ratio k_s/k_f varying from 2 to 10. Two types of boundary conditions were employed to numerically determine the dispersion coefficients, namely given temperatures and given heat fluxes. The main findings of this work are

(1) The type of boundary condition has little influence on the values of $(K_{dis})_{xx}$ and only a slight effect on $(K_{dis})_{yy}$ because temperature fields, within the fluid phase, are nearly equal when the two conditions are applied.
(2) Results of $(K_{dis})_{xx}$ are less sensitive to variations on porosity, ϕ, conductivity ratio, k_s/k_f, and medium morphology.
(3) Values of $(K_{dis})_{yy}$, instead, showed great sensitivity to medium morphology and the easier the fluid flows through the bed, permeating in a more streamlined structure (longitudinally-displaced elliptic rods), the lesser the dispersive mechanism for exchanging energy along the transversal y-direction.
(4) Porosity also affects $(K_{dis})_{yy}$ by obstructing the opening areas in the unit cells along the transversal direction, as ϕ decreases.
(5) Depending on ϕ, a higher conductivity ratio k_s/k_f reduces $(K_{dis})_{yy}$ for a certain Pe_H range and in situations where values of the spatial deviation ${}^iT$ are small, which occurs mainly within the recirculation regions behind the rods.

Acknowledgements

The authors are thankful to CNPq and FAPESP, for their financial support during the course of this research.

References

[1] C.T. Hsu, P. Cheng, Thermal dispersion in a porous medium, Int. J. Heat Mass Transfer 33 (1990) 1587–1597.
[2] M. Kaviany, Principles of Heat Transfer in Porous Media, second ed., Springer, New York, 1995.
[3] J.A. Ochoa-Tapia, S. Whitaker, Heat transfer at the boundary between a porous medium and a homogeneous fluid, Int. J. Heat Mass Transfer 40 (11) (1997) 2691–2707.
[4] C. Moyne, Two-equation model for a diffusive process in porous media using the volume averaging method with an unsteady-state closure, Adv. Water Resour. 20 (2–3) (1997) 63–76.

[5] A.V. Kuznetsov, L. Chena, M. Xionq, Effects of thermal dispersion and turbulence in forced convection in a composite parallel- plate channel: Investigation of constant wall heat flux and constant wall temperature cases, Numer. Heat Transfer; Part A: Appl. 42 (4) (2002) 365–383.
[6] P.-X. Jiana, Z.-P. Ren, B.-X. Wans, Numerical simulation of forced convection heat transfer in porous plate channels using thermal equilibrium and nonthermal equilibrium models, Numer. Heat Transfer; Part A: Appl. 35 (1) (1999) 99–113.
[7] P.-X. Jiang, B.-X. Wanq, D.-A. Luo, Z.-P. Ren, Fluid flow and convective heat transfer in a vertical porous annulus, Numer. Heat Transfer; Part A: Appl. 30 (3) (1996) 305–320.
[8] C.-H. Chen, Technical note: Non-Darcy mixed convection from a horizontal surface with variable surface heat flux in a porous medium, Numer. Heat Transfer; Part A: Appl. 30 (8) (1996) 859–869.
[9] M. Quintard, M. Kaviany, S. Whitaker, Two-medium treatment of heat transfer in porous media: numerical results for effective proprieties, Adv. Water Resour. 20 (2–3) (1997) 77–94.
[10] F. Kuwahara, A. Nakayama, Numerical modeling of non-Darcy convective flow in porous medium, in: Proceedings of 11th IHTC, vol. 4, Kyongju, Korea, 1998, pp. 411–416.
[11] A. Nakayama, F. Kuwahara, A macroscopic turbulence model for flow in a porous medium, ASME J. Fluids Eng. 121 (1999) 427–433.
[12] F.D. Rocamora, Heat Transport Modeling for Laminar and Turbulent Flows in Porous Media, Ph.D. Thesis, Instituto Tecnológico de Aeronáutica, Brazil, 2001.
[13] M.H.J. Pedras, F.D. Rocamora, M.J.S. de Lemos, Simulation of turbulent thermal dispersion in porous media using a periodic cell with prescribed heat flux at the boundaries, in: Proceedings of 3rd International Conference Computational Heat and Mass Transfer, May 26–30, Banff, Canada, 2003a.
[14] M.H.J. Pedras, F.D. Rocamora Jr., M.J.S. de Lemos, Turbulent dispersion in a porous media modeled as an infinite array of longitudinally-displaced elliptic rods, in: Proceedings of the COBEM2003 17th International Congress of Mechanical Engineering, November 10–14, São Paulo, Brazil, 2003b.
[15] M.H.J. Pedras, M.J.S. de Lemos, Turbulent dispersion in porous media modeled as an infinite array of transversally-displaced elliptic rods, in: Proceedings of the ICAPM 2004 2nd International Conference on Applications of Porous Media, May 24–27, Evora, Portugal, 2004.
[16] M.H.J. Pedras, M.J.S. de Lemos, On the definition of turbulent kinetic energy for flow in porous media, Int. Comm. Heat Mass Transfer 27 (2) (2000) 211–220.
[17] M.H.J. Pedras, M.J.S. de Lemos, Macroscopic turbulence modeling for incompressible flow through undeformable porous media, Int. J. Heat Mass Transfer 44 (6) (2001) 1081–1093.
[18] M.H.J. Pedras, M.J.S. de Lemos, Simulation of turbulent flow in porous media using a spatially periodic array and a low *Re* two-equation closure, Numer. Heat Transfer; Part A: Appl 39 (1) (2001) 35–59.
[19] M.H.J. Pedras, M.J.S. de Lemos, On mathematical description and simulation of turbulent flow in a porous medium formed by an array of elliptic rods, ASME J. Fluids Eng. 123 (4) (2001) 941–947.
[20] M.H.J. Pedras, M.J.S. de Lemos, Computation of turbulent flow in porous media using a low reynolds k–ε model and an infinite array of transversally displaced elliptic rods, Numer. Heat Transfer; Part A: Appl. 43 (6) (2003) 585–602.
[21] F.D. Rocamora, M.J.S. de Lemos, Analysis of convective heat transfer for turbulent flow in saturated porous media, Int. Commun. Heat Mass Transfer 27 (6) (2000) 825–834.
[22] M.J.S. de Lemos, M.H.J. Pedras, Recent mathematical models for turbulent flow in saturated rigid porous media, ASME J. Fluids Eng. 123 (4) (2001) 935–940.
[23] K. Abe, Y. Nagano, T. Kondoh, An improved k–ε model for prediction of turbulent flows with separation and reattachment, Trans. JSME, Ser. B 58 (1992) 3003–3010.
[24] S.V. Patankar, Numerical Heat Transfer and Fluid Flow, Hemisphere, New York, 1980.
[25] M. Saito, M.J.S. de Lemos, Interfacial heat transfer coefficient for non-equilibrium convective transport in porous media, Int. Commun. Heat Mass Transfer 32 (5) (2005) 667–677.
[26] M.B. Saito, M.J.S. de Lemos, A correlation for interfacial heat transfer coefficient for turbulent flow over an array of square rods, Journal of Heat Transfer 128 (5) (2006) 444–452.